I&EC research
Industrial & Engineering Chemistry Research

pubs.acs.org/IECR

Article

# Structure Evolution and Hoop-Reinforcing Mechanism of Bionic-Inspired Off-Axial Glass Fiber-Reinforced High-Density Polyethylene Pipes Fabricated via Rotating Co-extrusion

Rui Hong, Menglong Hu, Jin Chen, Qiang Fu, and Jie Zhang*

Cite This: https://doi.org/10.1021/acs.iecr.1c01455



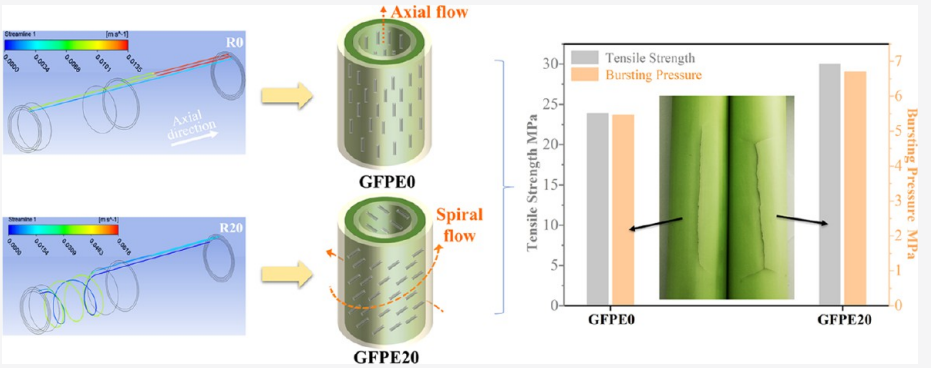


**ABSTRACT:** Triple-layer rotating co-extrusion is employed to fabricate hoop-enhanced polyethylene composite pipes with bionic off-axial glass fiber (GF)-reinforced high-density polyethylene (HDPE) middle layer. One kind of super-"hybrid shish-kebab"-like structures formed by GFs and interfacial lamellae tend to spirally align with a fiber deviation angle of 55.7° as the rotation rate reaches 20 rpm. Encouragingly, the hoop strength and hydraulic damage resistance are improved by 25.5 and 24.1%, respectively, even with a low fiber aspect ratio, which can be attributed to the enhanced hoop loading capacity and the energy dissipation effect of crack bifurcation contributed by deviated hybrid structures. Innovatively, the relationship between processing field and structure evolution has been systematically investigated by the simulation of melt flow track, shear rate, and flow rate, indicating that fiber deviation is closely related to the shear rate. This work develops a feasible strategy with both academic value and industrial application prospect for the hoop enhancement of fiber-reinforced HDPE pressure pipes and improves its adaptability to service requirements as well.

## 1. INTRODUCTION

Playing the role of "artery" in the lifeline of the city, high-density polyethylene (HDPE) pressure pipelines, such as water and gas pipelines, have usually been perceived as one of the important infrastructures in modern civilization owing to their outstanding long-term properties, excellent chemical resistance, and low cost.[1−4] For decades, the global population growth and increasing need for drinking water infrastructure have been expanding the demand for HDPE pipes with higher pressure resistance. Synchronously, a series of stricter standards toward higher-performance HDPE pipe resins have been incrementally established or further perfected nowadays.[5,6] Based on the continuous innovation of polymerization technology and stronger appreciation of the molecular structure modification, several generations of HDPE pipe materials have emerged including grade PE63, PE80, PE100, and PE125.[2,7] Nevertheless, these resins will inevitably face the stress distribution defect when used as pressure pipes, of which the hoop stress is twice as much as the axial stress.[8,9] This stress characteristic will bring the risk of bamboo-like splitting for conventional extruded pipes due to the axial arrangement (the extruding direction) of molecular chains. Commonly, reinforcing fiber, such as low-cost glass fiber (GF), is always utilized to improve the fracture strength of polymer products.[10,11] But, troubles still exist since the melt flow also arranges fiber fillers axially; thus, the reinforcement effect will only play an effective role in the axial rather than in the hoop direction.

Complex biological structures undergoing natural selection and evolution exhibit exceptional damage tolerance, which provides heuristic strategies to design the high-performance

Received: April 18, 2021
Revised: June 30, 2021
Accepted: June 30, 2021

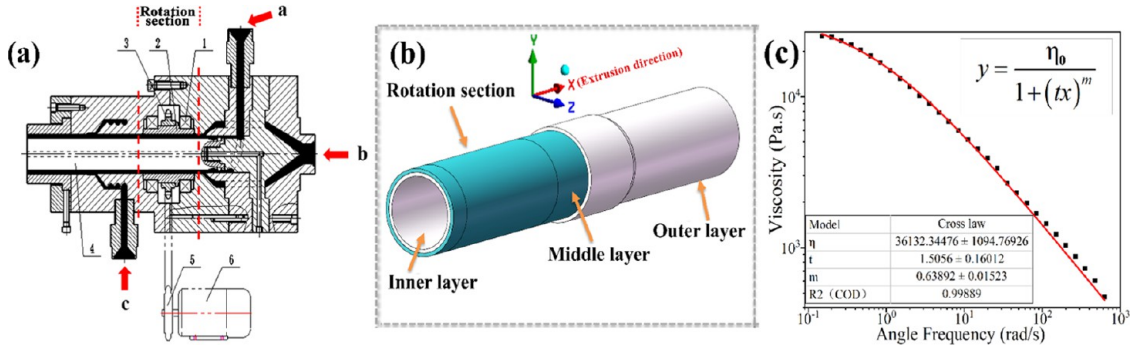


**Figure 1.** (a) Schematic diagram of the rotating co-extrusion device. 1—bearing; 2—rotation sleeve; 3, 5—sprocket; 4—mandrel; 6—electromotor. The red arrows a, b, and c are the entrances of melt for inner, middle, and outer layers, respectively. (b) The model of triple-layer composite pipe melt in the annular flow channel. (c) Viscosity−angle frequency curve and the cross-law fitting curve.

material structure, namely, bionic design.[12,13] For instance, the Bouligand structure of Stomatopods shows superior shielding ability against catastrophic crack propagation.[14,15] The spiral fiber alignment inspired by this structure points out the way for manufacturing fiber-reinforced composite pipe.[16] It is worth noting that a kind of spiral flow mandrel[17,18] has been widely used for polyolefin pipes to avoid weld lines through a short spiral flow induced by the spiral grooves on the mandrel surface. Nevertheless, the axial flow still dominates the whole flow path and the spiral flow only accounts for a small part. Accordingly, a rotary extrusion technology is proposed to realize the spiral fiber alignment by combining melt extrusion with an additional hoop-rotation shear field.[16,19−21] It has been demonstrated to be effective in improving hoop properties by forming off-axial alignment of oriented crystal structures in a variety of pipe products, including PE,[22] polypropylene (PP),[23,24] and polybutene (PB)[25] pipes. In those works, the hoop tensile strengths of PE, PP, and PB pipes increase by 45, 70.6, and 48.5%, respectively, by forming off-axially oriented cluster-like crystallite, hybrid shish-kebab, or in situ microfibers at mandrel rotation rates below 10 rpm. However, when the fiber filler is added, the single-layer composite pipe will possibly encounter the problems of floating fibers and the difficulty of butt fusion welding, leading to the generation of scales, the increase of fluid resistance, and the risk of weld fracture. In addition, further improvement of the hoop rotation rate is constrained because extremely high hoop components in the spiral compound flow field can induce serious flow instability. To solve the problem of floating fiber and improve weldability, we have proposed a triple-layer rotating co-extrusion strategy[26] to prepare pipes with the composite middle layer for reinforcement and the inner and outer layers made of neat resin for coating. Deng[26] elucidated that the hoop tensile strength of the GF-reinforced triple-layer polypropylene random copolymer pipe is successfully enhanced by 56.3% with the hoop rotation rate of 60 rpm. Due to the coating of neat resin layers, the pipe can be stably extruded and has an excellent surface quality even when the hoop rotation rate reaches up to 90 rpm, implying that the triple-layer rotary co-extrusion can provide a larger hoop flow component and higher productivity than the single-layer one.

The above endeavors demonstrated the multiscale structures oriented spirally during rotary extrusions, such as the fibrous filler or matrix crystal, can bring gratifying anisotropic properties. Visual computer simulation, which can deal with the complex polymer flow, is supposed to quantitatively reveal the relationship among the compound shear field, off-axial structure, and pipe performance. Li[19] and Yang[9] elucidated the gradient distribution of the shear and flow rates in annular channels with the hoop shear field, clarifying the correlation between the field condition and oriented structures (carbon fibers or shish-kebab structures). Nevertheless, the lack of systematic investigation on the extrusion process with adjusting hoop fields, which is critical to guiding the fabricating of high-performance pipes in the industry field, still calls for a further and comprehensive investigation of flow simulation. Meanwhile, the interface bonding between fiber fillers and matrix,[27,28] one of the key elements for mechanical properties of composites, has not been paid enough attention by those researchers.

In the current work, the triple-layer rotating co-extrusion technology was applied to prepare the hoop-enhanced HDPE composite pipe with the inner and outer layers made of neat HDPE and the middle layer made of GF/HDPE. The multiscale structures, including reinforcing fiber and matrix crystals, evolved with the gradient growth of the rotation rate and have been analyzed and discussed in three observation planes; their influence on pipe properties has also been studied in detail. Furthermore, the melt flow track, shear rate, and flow rate under various conditions are obtained via flow simulation, and the quantified relationship between the external field and the inner structure is established. As will be clarified, the hoop performances of pipes are effectively enhanced by the spiral alignments of GF, and interfacial lamellae deviated from the axial direction at the corresponding rotation rate. This strategy paves the way for the industrial fabrication of high hoop-performance HDPE composite pipes with enhanced hydraulic damage resistance.

## 2. EXPERIMENTAL SECTION

**2.1. Materials.** The HDPE (PE100, trade name 4902T, with a density of 0.95 g/cm$^3$ and a melt flow rate of 0.23 g/10 min under the pressure of 5 kg at 190 °C) was commercially available from Yangzi Petrochemical Company Limited (China). The short-cut glass fiber (ESC13-4.5-508A, with a fiber diameter of ∼13 μm and a fiber length of ∼4.5 mm) was purchased from Jushi Group Co. (China). The fiber was used without any pretreatment.

**2.2. Device and Sample Preparation.** A schematic diagram of a triple-layer rotating co-extrusion device is shown in Figure 1a. Three single-screw extruders are employed to provide melts (the parameters of extruders are listed in Table S1). In a typical triple-layer rotating co-extrusion, the inner


https://doi.org/10.1021/acs.iecr.1c01455
Ind. Eng. Chem. Res. XXXX, XXX, XXX−XXX

**Table 1. Flow Boundary Condition Parameters of Melt Flow in Machine Head**

| model layer | volume flow rate of each layer ($m^3/s$) | fitted melt parameters | | simulated flow processes | $V_t$ on the rotating surface (m/s) |
|---|---|---|---|---|---|
| inner layer | $2.39 \times 10^{-6}$ | zero shear viscosity | 36 132.3 Pa·s | R0 | 0 |
| | | | | R5 | 0.15 |
| middle layer | $2.71 \times 10^{-6}$ | natural time | 1.5 s | R10 | 0.31 |
| | | | | R20 | 0.62 |
| outer layer | $2.74 \times 10^{-6}$ | cross-law index | 0.64 | R50 | 1.55 |
| | | | | R70 | 2.16 |

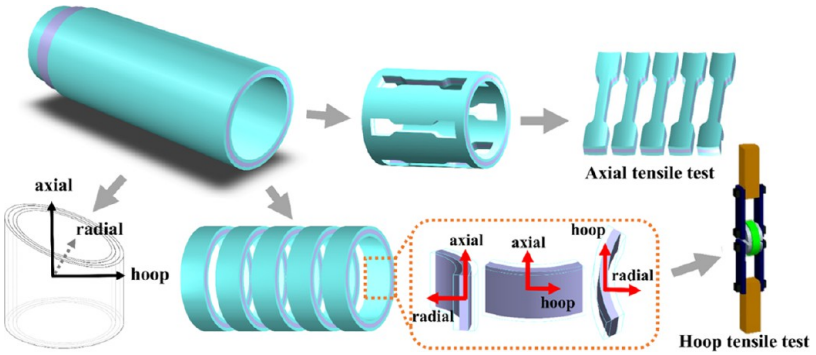


**Figure 2.** Schematic diagram of sampling the test specimens from triple-layer pipes.

layer and middle layer melts first converge to form the double-layer pipe melt. It moves to the rotation section and undergoes a hoop shear field imposed by the rotation sleeve subsequently. Finally, the double-layer pipe melt will be coated by the outer layer after rotation shearing and extruded through the die.

The raw GF/HDPE composite pellets of the middle layer were prepared through the twin-screw extruder (Coperion STS-35) with a fiber content of 40 wt %, during which the barrel temperature of the extruder was set at 170−200 °C from hopper to die and with a screw speed of 400 rpm. Neat HDPE was applied for inner and outer layers as stated above. The temperature from hopper to rotating co-extrusion device would be preset at 170−220 °C before the pipe preparing process. The balance of extrusion and the expected thickness of each layer is achieved by controlling their melt-conveying rates by adjusting the screw speed of each extruder. Specifically, the screw speed of the middle-layer extruder is 350 rpm and the screw speeds of inner and outer layer extruders are both 310 rpm. In addition, various hoop shear fields were provided by applying the rotational rates of 0, 5, 10, 20, 50, and 70 rpm, respectively. Once extruded from the die, the pipe blanks were immediately sized by negative pressure and cooled by external spray, and finally collected. The outer diameter of the pipe was 50 mm, with the thicknesses of the outer layer, middle layer, and inner layer kept at 1.3, 2, and 1.3 mm, respectively. In brief, these samples were named GFPE0, GFPE5, GFPE10, GFPE20, GFPE50, and GFPE70, respectively.

**2.3. Flow Simulation.** The melt flow behavior in the annular channel of a triple-layer pipe was simulated using Polyflow. As depicted in Figure 1b, a flow model with triple-layer subdomains interconnected through fixed interfaces was built. The inlets of the inner and middle layers were set at their confluence point to simplify the flow model, while the outer layer inlet was set at the beginning of coating. The rotation section was defined to exert the hoop shear fields. Taking the Cartesian axis (0, 0, 0)−(1, 0, 0) as the rotation axis, namely, the central axis of the model, various tangential velocities could be endowed on the rotation section boundary. In particular, a no-slip condition was assumed between the melt and the channel walls. The melt velocity at the model boundary could be as follows:

On the stationary surface of the channel wall, $V_n = V_t = 0$
On the rotating surface of the rotation sleeve, $V_n = 0$ and $V_t = 2\pi nr$

where $V_n$ and $V_t$ are the normal velocity and tangential velocity of the polymer melt, respectively, $n$ is the rotation rate (in rpm), and $r$ is the radius of the rotation sleeve surface (in mm).

Moreover, the generalized Newtonian fluid constitutive equation combined with the cross-law for shear-rate dependence of viscosity was used to deal with the flow behavior

$$T = 2\eta(T, \dot{\gamma})D \tag{1}$$

$$\eta = \frac{\eta_0}{1 + (\lambda\dot{\gamma})^m} \tag{2}$$

where T is the extra-stress tensor; $D$ is the rate-of-deformation tensor; $\eta$ is the shear viscosity and is a function of the local shear rate $\dot{\gamma}$, the temperature $T$, or both; $\eta_0$ is the zero-shear-rate viscosity; $\lambda$, the nature time, is the inverse of the shear rate at which the melt changes from Newtonian to power-law behavior; and $m$ is the cross-law index.

The model boundary conditions and the fitted rheological parameters are listed in Table 1. Based on the practical extrusion experiment, these simulated flow processes were designated as *Rx*, where *x* means the chosen rotation rates. As displayed in Figure 1c, the rheological curve at 220 °C was fitted by the cross-law after conversion according to the Cox−Merz rule. The flow problem was simplified by neglecting gravity, inertia terms, and viscous heating during simulation. The steady-state method, the Picard iterations on viscosity, and the mean least-squares technique were adopted for computing the flow rate and the shear rate.

**2.4. Characterization.** *2.4.1. Polarization Light Microscopy.* Polarization light microscopy (PLM) was adopted to observe the residual length distribution of GF in GF/HDPE raw pellets and the fiber arrangement in pipes. The composite


https://doi.org/10.1021/acs.iecr.1c01455
Ind. Eng. Chem. Res. XXXX, XXX, XXX−XXX

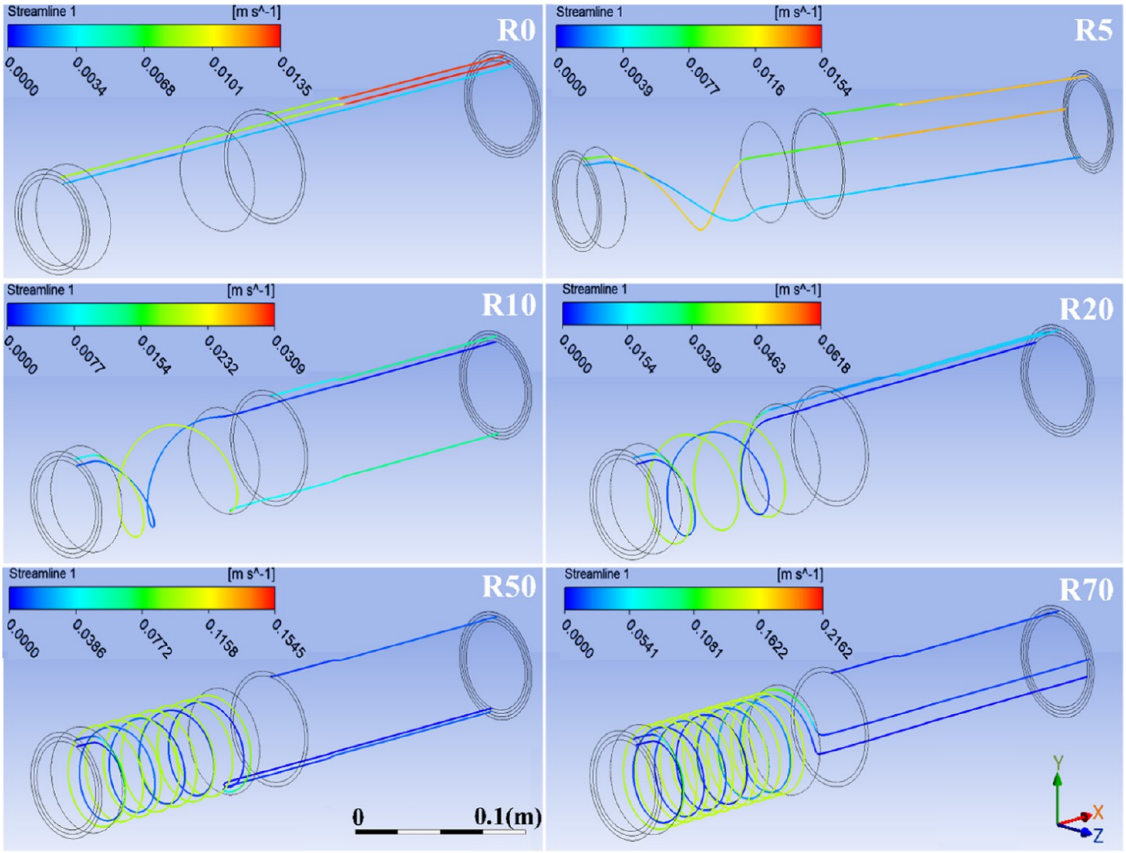


**Figure 3.** Melt flow tracks of the triple-layer pipe melt during the rotating co-extrusion processes.

pellets were hot-pressed into thin films with a thickness of 50 $\mu$m at 200 °C beforehand, and slices with a thickness of 30 $\mu$m along the hoop-radial plane (see Figure 2) of pipes were cut by microtome. The optical observation was performed using the optical microscope (DX-1, Phoenix Optical Co., China) equipped with a camera (Nikon 500D digital camera).

*2.4.2. Dynamic Rheological Characterization.* The HDPE and GF/HDPE pellets were hot-pressed into disklike rheological samples with a thickness of 1 mm and a diameter of 20 mm for 5 min at 190 °C and 10 MPa and then cooled at 25 °C and 10 MPa for another 5 min. The dynamic frequency sweep was carried out at 220 °C on a parallel plate rotary rheometer (Thermo Scientific MARS III, Haake, Karlsruhe, Germany) with a strain of 1% and an angle frequency between 0.63 and 628.3 rad/s.

*2.4.3. Differential Scanning Calorimeter.* The thermal behavior of the raw pellets and pipe samples (5−8 mg) were analyzed using a differential scanning calorimeter (DSC) (TA Q200) device under a nitrogen atmosphere. For raw materials, the heating−cooling−heating mode was adopted to eliminate thermal history. Each sample was first heated from 40 to 200 °C with a heating rate of 50 °C/min and maintained for 10 min, and then cooled to 40 °C with a cooling rate of 10 °C/min. Subsequently, they were heated to 200 °C for the second time with a rate of 10 °C/min. While, with respect to pipe samples, the melting behavior of each layer was investigated by heating from 40 to 200 °C with a rate of 10 °C/min. Crystallinity was determined by normalizing the integral of the enthalpy peak from 60 to 180 °C with the melting enthalpy of 100% crystalline polyethylene (291 J/g).

*2.4.4. Mechanical Properties and the Hydraulic Burst Test.* The axial and hoop mechanical properties were tested on a universal testing machine (Instron 5567) with a cross-head speed of 20 mm/min at 25 °C according to ASTM D638-14. The mechanical test specimens and the clamp sketch of the hoop tensile test are exhibited in Figure 2. Among them, the axial mechanical test specimens were in dumbbell shape, with a narrow section size of 20 mm × 4 mm × wall thickness (~4.6 mm); the ring specimens with a width of 13 mm were cut for the hoop mechanical test. Not less than five specimens are tested in each category.

In the hydraulic burst test, 1 m pipes were put in water at a constant temperature of 20 °C for 1 h and then pressurized at both ends with a growth rate of 0.5 MPa/s until the pipes burst.

*2.4.5. Scanning Electron Microscopy.* Scanning electron microscopy (SEM) characterization was performed using an FEI (Nova Nano SEM450) SEM device on the cross section of hoop-axial, hoop-radial, and axial-radial planes (Figure 2). The observation surface was polished with 7000 mesh sandpaper and then immersed into an etch solution at 60 °C for 7 h to remove the amorphous phase selectively. Then, it underwent the gold sputtering treatment before SEM characterization. Each 200 mL etch solution contained sulfuric acid, phosphoric acid, and distilled water (content ratio of 10:4:1), and 3 g of potassium permanganate.

## 3. RESULTS

**3.1. Flow Simulation Results.** The melt flow tracks and the flow rate range during rotating co-extrusion are principally analyzed according to the simulation results. As displayed in


https://doi.org/10.1021/acs.iecr.1c01455
Ind. Eng. Chem. Res. XXXX, XXX, XXX−XXX

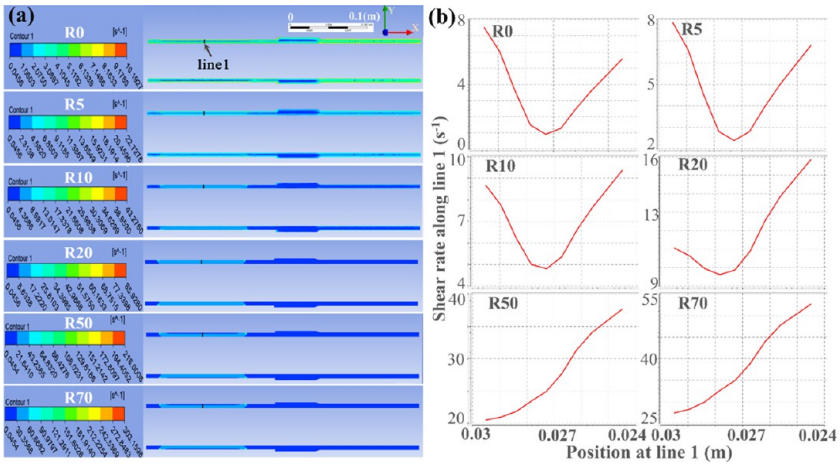


**Figure 4.** (a) Contours of shear rate distribution in the $X-Y$ axis section of the triple-layer pipe blanks and (b) the shear rate curves along line 1 during the rotating co-extrusion processes.

Figure 3, these tracks start from the radial midpoint of each layer at the inlet. As the hoop shear field is introduced, the melt flow in the rotation section shifts from the axial flow (R0) to spiral flow (R5−R70) for the middle and inner layers, but the outer layer melt invariably flows along the axial direction in the coating step. One can observe from the contour colors that the maximum melt rate increases from 0.014 m/s for R0 to 0.216 m/s for R70, and the maximum rate region is transferred from the outlet vicinity to the outer wall of the rotation section. Simultaneously, the pitch of the spiral flow diminishes, yet the flow distance and the cycle number increase. These variations confirm that a high rotation rate will enhance the flow rate by endowing the melt with a greater hoop rate component. The flow rate drops to zero at the inner wall of the flow model according to the no-slip condition, avoiding the formation of rotation mark defects.

The shear rate, defined as the flow rate discrepancy between adjacent microfluidic layers, reflects the gradient variation of the flow rate. Figure 4a depicts the shear rate contours of pipe melts in the $X-Y$ axis section. The high shear rate region also moves with the exerting of the hoop shear field as does the flow rate. Under R0 and R5 conditions, these regions appear close to the channel walls of the whole model, but when the rotation rate exceeds 5 rpm, the shear rate at the rotation section is higher than in other areas.

To further investigate the radial distribution of the shear rate, a radial section line at the midpoint of the rotation section (see line 1 in Figure 4a) was drawn and the shear rate along it was recorded, as in Figure 4b. Shear rates at positions 0.295, 0.270, and 0.245 m, corresponding to the outer wall, inter interface, and the inner wall of the rotating double-layer model, are shown in Table 2. The shear rates on the outer and inner walls of the middle layer increase remarkably from 7.5 and 1.2 $s^{-1}$ for R0 and up to 27.1 and 36.9 $s^{-1}$ for R70, benefiting from the amplified hoop field component. Moreover, the shear rate in the inner layer shows a more rapid promotion due to the higher velocity discrepancy between microfluidic layers caused by the inner-wall sticking effect. Together, those results reveal adequate quantitative data for the shear field of rotating co-extrusion and provide valuable references for analyzing the multiscale structure evolution in pipes.

**3.2. Experimental Results.** *3.2.1. Residual Fiber Length.* Figure 5 shows the PLM image of GF/HDPE composite pellets and the length distribution of residual fibers randomly

**Table 2. Shear Rates at Positions 0.295, 0.270, and 0.245 m along Line 1**

| | shear rate at positions along line 1 ($s^{-1}$) | | |
|---|---|---|---|
| simulated flow processes | 0.295 m | 0.270 m | 0.245 m |
| R0 | 7.5 | 1.2 | 5.6 |
| R5 | 7.8 | 2.6 | 6.8 |
| R10 | 8.7 | 5.1 | 9.4 |
| R20 | 11.1 | 10.4 | 15.8 |
| R50 | 20.3 | 26.3 | 37.4 |
| R70 | 27.1 | 36.9 | 52.5 |

counted by Imagepro. As expected, the twin-screw extruder has an excellent mixing efficiency on the composite system, but the strong shear stress exerted by the twin-screw shearing[29] and the granulation cutting[30] may lead to the undesirable fracture of GFs, which may cause a lower reinforcement efficiency.[31] In our case, the average residual length of GF in pellets is 118 $\mu$m, which means only 2.6% of the original length (~4.5 mm) has been kept. Nearly half of the fibers are between 75 and 100 $\mu$m. According to the critical fiber length theory given by Kelly and his colleagues,[32,33] the aspect ratio of the critical fiber length $l_c$ and fiber diameter $d$ is defined as

$$\frac{l_c}{d} = \frac{\sigma}{2\tau} \tag{3}$$

where $\sigma$ is the intrinsic strength of the reinforcing fiber and $\tau$ is the interfacial shear strength. Fibers with a length below $l_c$ will not carry the load matching their intrinsic strength, implying that some of them will be pulled out instead of breaking while the product fractures. Despite no accurate critical aspect ratio reported for GF/HDPE systems, we have learned that more than 30 wt % glass fibers with aspect ratio of 15.7 can only show a slightly reinforcement.[34] The GF diameter here is ~13 $\mu$m, so the average aspect ratio is 9.1, implying that the majority of residual fibers have lower aspect ratios than the above-mentioned case. That is, this length level of the residual fiber may hardly provide us with an expectation of effective reinforcement.

*3.2.2. Mechanical Property and Hydraulic Damage Resistance.* Figure 6a,b depicts the hoop and axial mechanical properties of the rotating co-extruded triple-layer pipes with the GF/HDPE composite middle layer. The hoop tensile


https://doi.org/10.1021/acs.iecr.1c01455
Ind. Eng. Chem. Res. XXXX, XXX, XXX−XXX

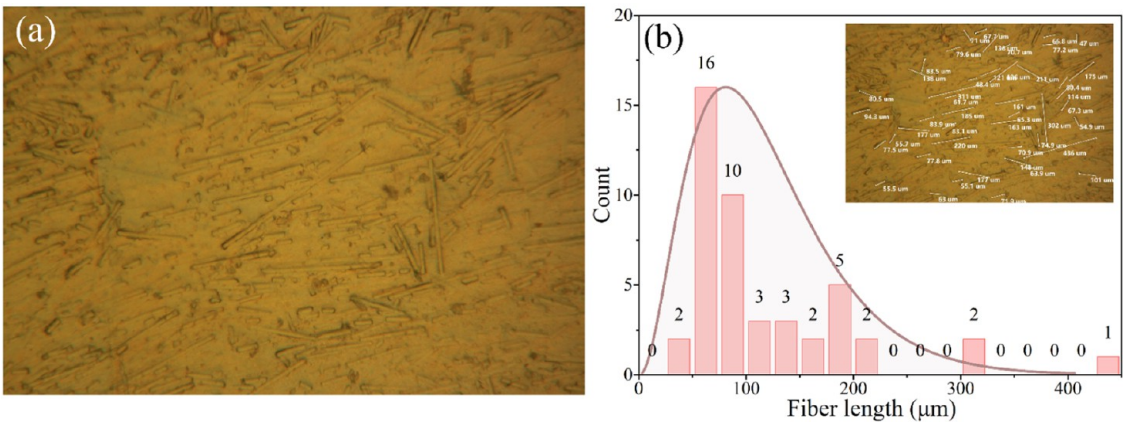


**Figure 5.** (a) PLM image of film hot-pressed from GF/HDPE composite pellets and (b) length and distribution of residual fibers counted from the PLM image.

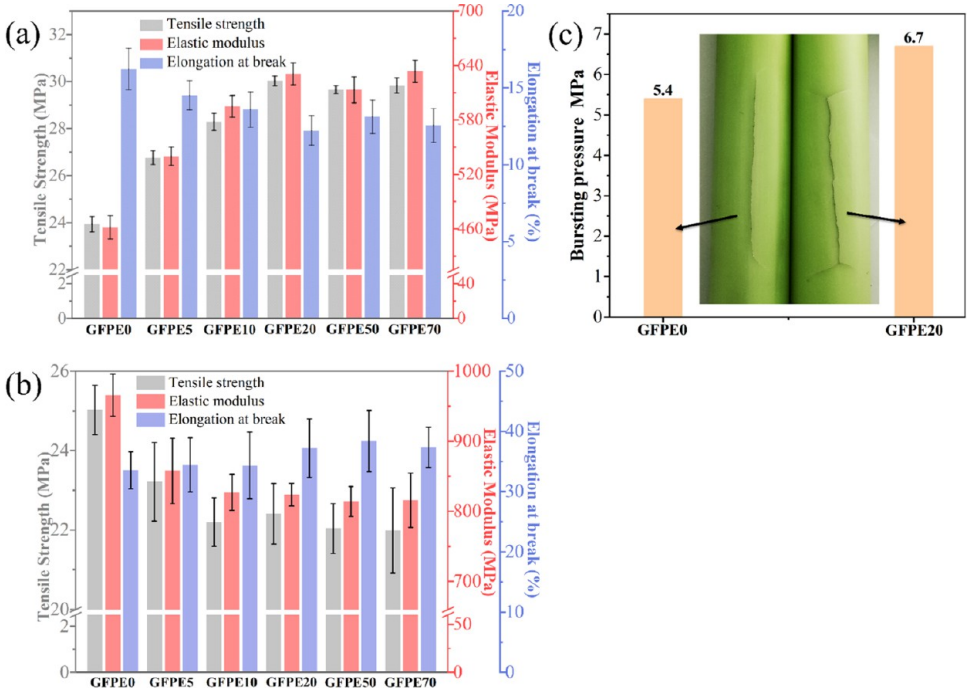


**Figure 6.** (a) Hoop mechanical properties and (b) the axial mechanical properties of pipes prepared with various rotation rates. (c) Bursting pressures and failure modes of GFPE0 and GFPE20.

strength and hoop elongation at break of GFPE0 are 23.9 MPa and 16.2%, respectively, while its tensile modulus is 461.7 MPa, which is only able to be compared parallelly in our study as a calculated value. As also can be noticed, the hoop tensile strength and modulus of pipe begin to increase with the rotation rate increasing. The hoop tensile strength of GFPE20 reaches 30.0 MPa with an increment of 25.5% in comparison to GFPE0; meanwhile, the corresponding tensile modulus is improved by 36.9%. Once the rotation rate exceeds 20 rpm, both of them do not change much anymore. Nevertheless, those results are still inspiring because they verify the reinforcing effect of GFs on the hoop mechanical properties in spite of the relative low aspect ratio. Instead, the hoop elongation at break shows a downward trend with the increase of the rotation rate.

Changes in the axial mechanical properties with the rotation rate show an opposite trend to that of the hoop mechanical properties. After applying the hoop shear at a rotation rate of 10 rpm, the axial tensile strength and modulus decrease from 25.0 and 965.8 MPa to 22.2 and 827.0 MPa for GFPE0. For GFPE20 with the maximum hoop tensile strength, the axial tensile strength and modulus are 10.5 and 14.7% lower, respectively, those of GFPE0. Meantime, the axial elongation at break increases from 33.5% for GFPE0 to 37.2% for GFPE20.

Given that the optimal hoop reinforcement appears at the rotation rate of 20 rpm, the bursting test is adopted to compare the hydraulic damage resistance of GFPE20 and GFPE0. As shown in Figure 6c, the burst pressure increases from 5.4 MPa of GFPE0 to 6.7 MPa of GFPE20 with an amplification of 24.1%. The bursting crack of GFPE0 develops along the axial direction, while the axial growth of the GFPE20 crack seems to be hindered, forming hoops extending branches at both ends of the crack. This evolution in crack growing behavior will help dissipate the crack growth energy and prevent the axial crack propagating to a larger distance. To sum up, the additional


https://doi.org/10.1021/acs.iecr.1c01455
Ind. Eng. Chem. Res. XXXX, XXX, XXX−XXX

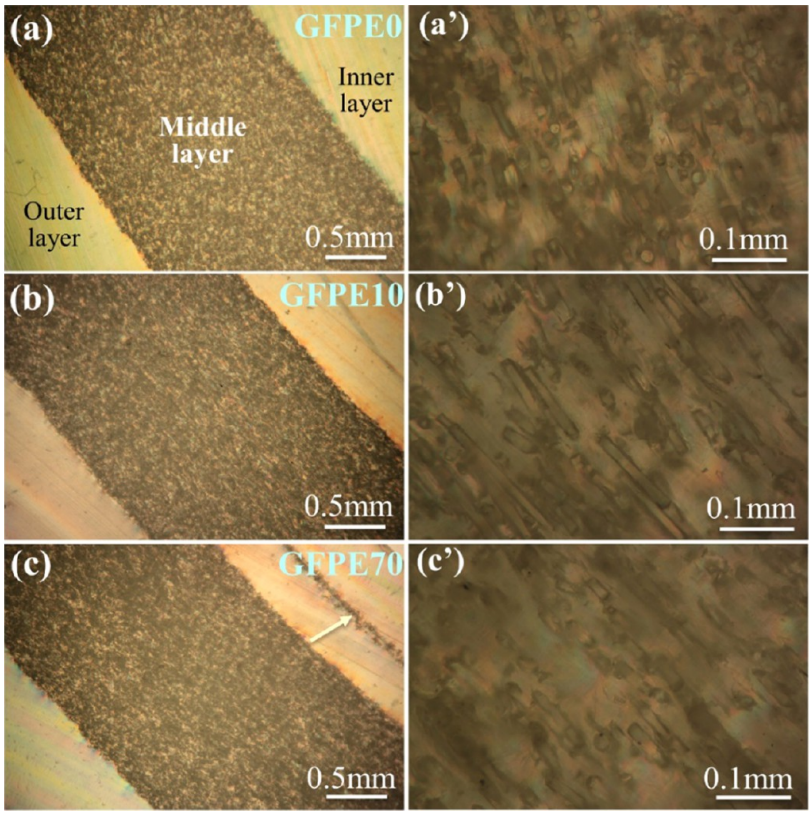


**Figure 7.** PLM images of pipes observed in the hoop-radial plane: (a, a′) GFPE0, (b, b′) GFPE10, and (c, c′) GFPE70.

hoop shear field indeed plays an effective role in the enhancement of hoop strength and hydraulic damage resistance.

*3.2.3. Fiber Distribution Evolution.* It has been well accepted that mechanical properties of polymer products are greatly determined by the inner multiscale structure. To clarify the mechanism for hoop enhancement, the microstructure, including GF distribution and matrix morphology of pipes, is analyzed.

Figure 7 displays the PLM images observed in the hoop-radial plane of pipes. The GFs in the middle layer of GFPE0 (see Figure 7a,a′) are presented in dot formation, that is, they are perpendicular to the observation plane, or axially oriented. But for GFPE10 (Figure 7b,b′) and GFPE70 (Figure 7c,c′), the GFs are dispersed in a linear formation, indicating that the fibers have deviated from the axial direction. Moreover, it is obvious that, in GFPE70, a small number of fibers migrate to the inner layer (marked by the arrow), and the reasons will be discussed in the following section.

The SEM images at the outer wall of the middle layers of the pipes observed in the hoop-axial plane are depicted in Figure 8. It is easily seen that GFs are uniformly arranged along the axial direction in GFPE0. As the rotation rate increases to 20 rpm, the GFs in the visual field are gradually deviated from the axial direction, indicating that the fibers are spirally aligned in the pipe as expected. Here, the average angles by which fibers deviate from the axial direction are counted randomly. Consistent with the variation trend of the hoop performance, the fiber deviation angle reaches up to 55.7° for GFPE20 but does not increase any more with a higher rotation rate. Thus, we can reasonably infer that the hoop property of the pipe is highly correlated with the deviation of GFs that the aligned fibers may have a superior load-bearing capacity in their orientation direction.[35]

To further explore the radial distribution of the GF arrangement, the hoop-radial and axial-radial planes of pipes are also characterized by SEM, as shown in Figure 9. The dot-formed fibers in the hoop-radial plane of GFPE0 (Figure 9a,a′) imply that GFs are oriented along the axial direction. As for the GFPE10 (Figure 9b,$b_1$′,$b_2$′), the GFs are dispersed as short lines extending out of the matrix. It is easy to identify the off-axial GFs, although some of them are abraded during sample polishing. Furthermore, an obvious radial distribution discrepancy of fiber deviation exists in the hoop-radial plane of GFPE70 (Figure 9c), that is, the fibers close to the outer layer (Figure 9$c_1$′) and inner layer (Figure 9$c_2$′) are shown as short linear and long linear, respectively. The idealized fiber orientation diagram (Figure 9g) provides a better explanation of the GF orientation state, in which scattered dots, short lines, or long lines represent fibers parallel, deviated, or perpendicular to the normal of the section, respectively. As expected, the above-mentioned orientation distribution of GFs is well matched in the axial-radial plane (Figure 9d−f). Especially for GFPE70 (Figure 9f,$f_1$′,$f_2$′), the short-line and dot-distributed GFs can be found right by the outer wall and inner wall of the middle layer, respectively; among them, the latter has a greater deviation. Undoubtedly, the off-axial fiber alignment with "bionic spiral bouligand structure" is successfully formed through spiral melt flow in rotating co-extrusion. In addition, the SEM results also present the migrated fibers in the inner layer of GFPE70 (Figure 9c,f), which has been verified in PLM observation.

*3.2.4. Matrix Crystal Evolution.* It is well established that product properties are also affected by matrix crystallization behaviors under the action of an external field.[36−39] DSC


https://doi.org/10.1021/acs.iecr.1c01455
Ind. Eng. Chem. Res. XXXX, XXX, XXX−XXX

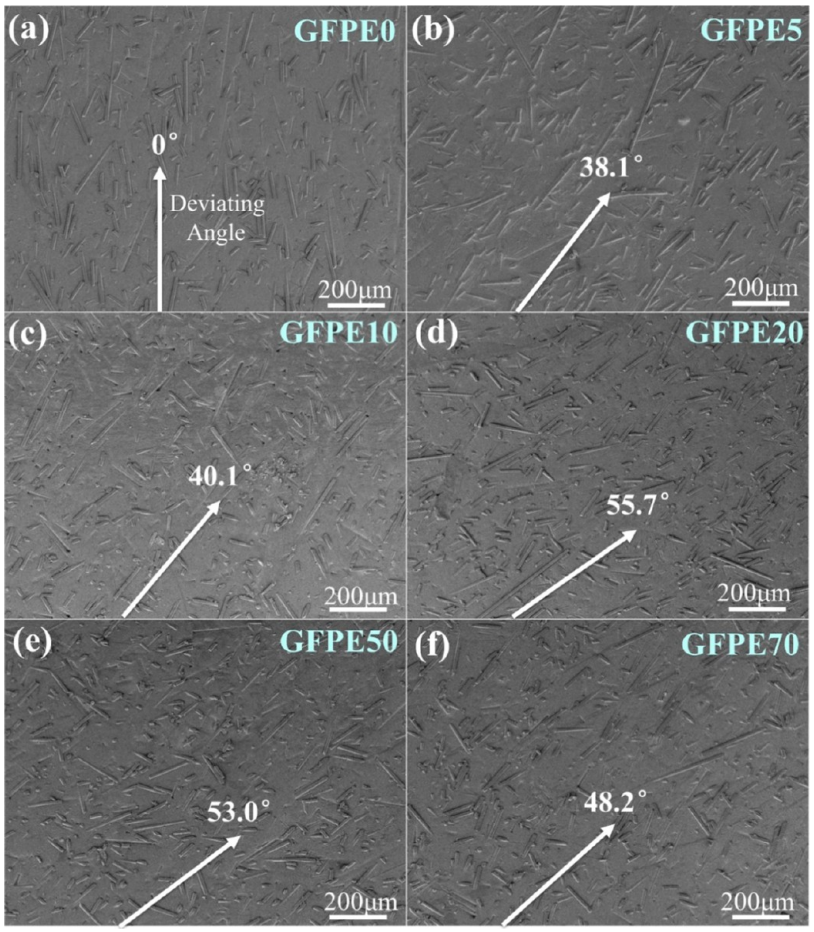


**Figure 8.** GF distributions in the hoop-axial plane of the GF/HDPE middle layers (magnification of ×150): (a) GFPE0, (b) GFPE5, (c) GFPE10, (d) GFPE20, (e) GFPE50, and (f) GFPE70. The arrows indicate the average deviation angle of GFs, which are arranged along the axial direction in GFPE0.

measurements were conducted to visualize the thermal property, and, herein, the melting curves and crystallization information of raw materials and each pipe layer are available in Figure 10 and Table 3 for comparison. Obviously, in contrast to the HDPE raw pellet, the GF/HDPE pellet has a higher melting temperature ($T_m$) but a slightly lower crystallinity ($X_c$). From the pipe perspective, $T_m$ shows a slightly increasing trend from the outer to inner layer overall because it is highly dependent on the distribution of the temperature field in which the cooling rate of the inner layer is slower than that of the outer layer, and is referred to the heat conduction effect of the multilayer wall.[40] Due to the fastest cooling rate, the outer layer experiences the shortest crystallization time, thus showing both the lowest $T_m$ and $X_c$. However, the highest $X_c$ appears in the middle layer instead of the inner layer, which is not consistent with the trend of $T_m$. In addition, under the action of the hoop shear, the $X_c$ of the middle layer increases from 70.6% for GFPE0 to 79.2% for GFPE70, but the homologous variation does not occur in the inner layer. Thus, we can rationally infer that the fibers play a key role in the process of shear promoting matrix crystallization.

For raw pellets, the $T_m$ and $X_c$ of HDPE are 132.4 °C and 73.4%, and the $T_m$ and $X_c$ of GFPE are 134.8 °C and 72.2%, respectively.

Considering the fiber deviation responding to the hoop shear and the subsequently promoted matrix crystallization, the corresponding crystal morphology is also worth further studying. Figure 11 depicts the etched crystal morphology in the axial-radial plane. Clearly, at the interface where GFs are detached during the grinding or etching process, the crystal morphology is quite different from that inside the matrix. In general, the HDPE lamellae are randomly distributed inside the matrix but form oriented lamellae at the interface. For samples prepared at a low rotation rate (GFPE5 and GFPE10), there seems to be no obvious deviation of interfacial lamellae, which lags behind that of GF. Nevertheless, the interfacial lamellae deviation becomes pronounced when the rotation rate reaches 20 rpm, concurrent with the increase of the hoop tensile strength; thus, the interfacial lamellae deviation may also account for the pipe properties besides reinforcing fibers. The lamellae deviation is also confirmed in the hoop-radial plane and the axial-radial plane (Figure S2), where the hoop orientation becomes remarkable and the axial orientation fades gradually with the increased rotation rate.

## 4. DISCUSSION

The above results demonstrate that the spirally oriented microstructures combined with increased crystallinity are obtained in the middle layer with the introduction of a hoop shear field during co-extrusion, and, as a result, the hoop strength and hydraulic damage resistance of pipes are successfully improved. In this section, we will try to reveal


https://doi.org/10.1021/acs.iecr.1c01455
Ind. Eng. Chem. Res. XXXX, XXX, XXX−XXX

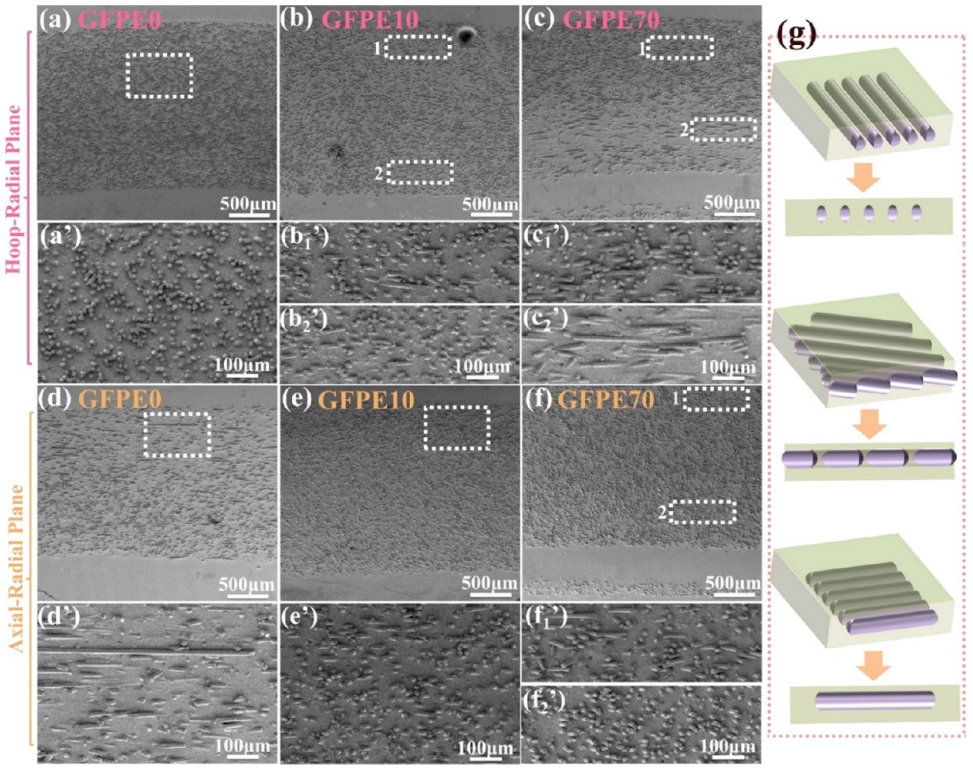


**Figure 9.** GF distributions in the (a–c) hoop-radial plane and (d–f) axial-radial plane of pipes. The outer, middle, and inner layers are from top to bottom. Images (a′–$f_2$′) are magnified from the rectangle areas in (a–f). (g) Schematic diagram of three kinds of idealized fiber arrangements within the matrix and at section.

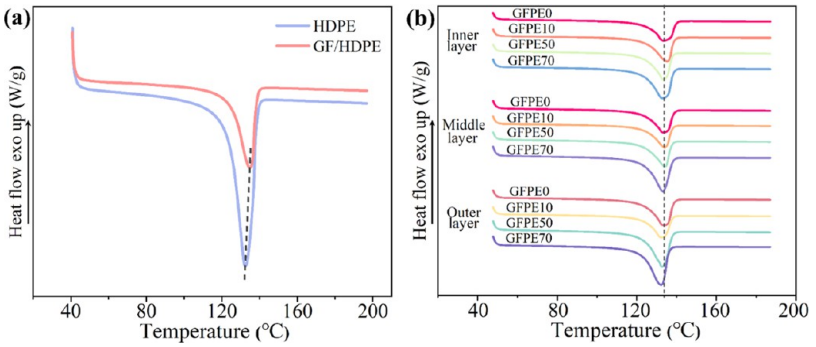


**Figure 10.** DSC curves of (a) raw pellets and (b) each layer of pipes prepared with different rotation rates.

**Table 3. Melting Point and Crystallinity of Raw Pellets and Each Layer of Pipes**

| | inner layer | | middle layer | | outer layer | |
|---|---|---|---|---|---|---|
| pipe samples | $T_m$ (°C) | $X_c$ | $T_m$ (°C) | $X_c$ | $T_m$ (°C) | $X_c$ |
| GFPE0 | 133.4 | 69.0 | 133.3 | 70.6 | 133.8 | 64.9 |
| GFPE10 | 135.2 | 69.9 | 133.9 | 71.7 | 132.5 | 65.9 |
| GFPE50 | 133.2 | 72.0 | 134.2 | 72.2 | 132.7 | 65.7 |
| GFPE70 | 133.1 | 69.2 | 133.1 | 79.2 | 132.1 | 65.4 |

the microstructure evolution mechanism behind the performance enhancement of rotating co-extruded pipes.

First, how the microstructures evolve in the controlled shear field must be clarified. The simulated melt flow rates along the radial section line 1 (see Figure 4a) are recorded in Figure S1. Similar to the gradually increased shear rate, the flow rate on the outer wall of the rotating model also shows a growing tendency, which increases from 0 m/s for R0 to the maximum of 0.216 m/s for R70. However, in Figure 8, the GF deviation angle on the outer wall of the middle layer slightly decreases when the rotation rate exceeds 20 rpm, which does not keep in line with both the field parameters above. So why does fiber deviation angle decrease at a high rotation rate? In fact, the answer can be drawn from the discussion on the radial distribution of GFs in GFPE70. The SEM images of GFPE70 (Figure 9c,$c_1$′,$c_2$′) show that some GFs migrate into the inner layer, and more pronounced fiber deviation occurs near the inner wall rather than the outer wall of the middle layer. While for simulated R70 conditions, the inner layer possesses higher shear rates but lower flow rates than the middle layer. Therefore, it is clear that the shear rate plays a greater role in fiber deviation than the flow rate; otherwise, the larger deviation angle should appear on the outer wall of the middle layer. Thus, the gradually increased deviation angle of GF should be attributed to the incremental shear rate before the rotation rate reaches 20 rpm. Meanwhile, it can also be


https://doi.org/10.1021/acs.iecr.1c01455
Ind. Eng. Chem. Res. XXXX, XXX, XXX−XXX

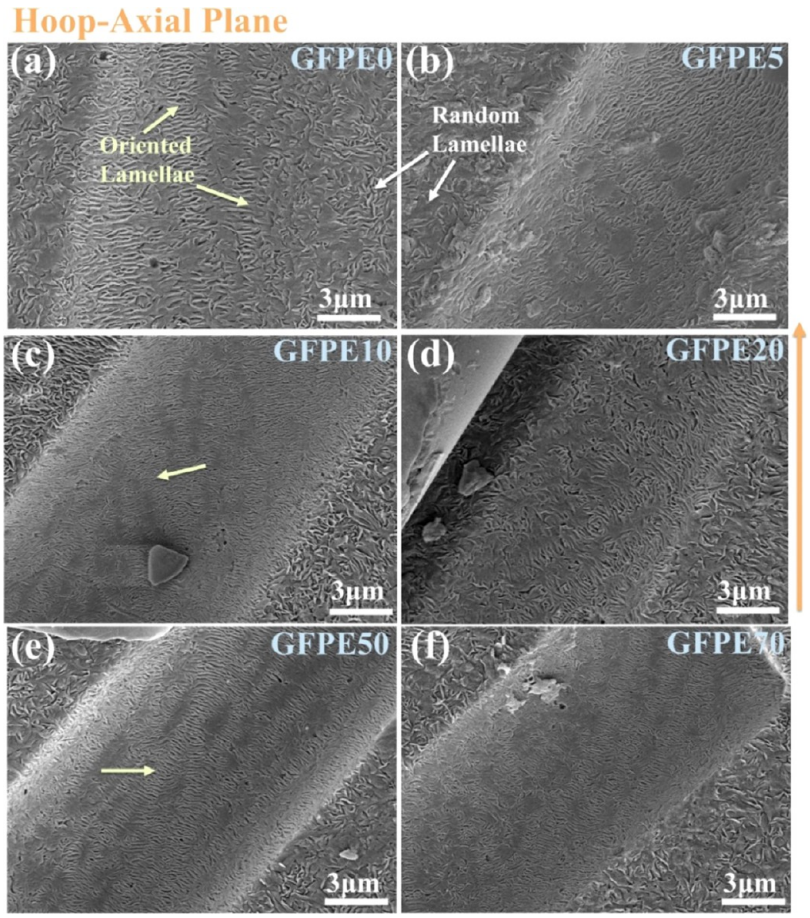


**Figure 11.** Morphologies in the hoop-axial plane of the GF/HDPE middle layers (magnification of ×12 000): (a) GFPE0, (b) GFPE5, (c) GFPE10, (d) GFPE20, (e) GFPE50, and (f) GFPE70. The upward arrow points in the axial direction.

reasonably inferred that the slight decrease of the deviation angle at a higher rotational rate is independent of the high flow rate itself, but is possibly due to the local instable flow caused by the high rotational rate, which cannot reflect the true rate discrepancy between microfluidic layers in practical cases.

The GF not only plays a key role in the process of shear promoting matrix crystallization for the middle layer but also impacts on the matrix crystal morphology. Herein, the HDPE lamellae are oriented at the interface and randomly distributed inside the matrix for all samples (see Figures 11 and S2); thus, we can draw a conclusion that the influence of fiber on crystallization is mainly close to the interface. To illustrate the function of GF, the dynamic rheological sweeps are employed for raw materials and the storage and loss modulus ($G'$ and $G''$) curves are available in Figure S3. The frequency at the intersection of the $G'$ and $G''$ is inversely related to the characteristic relaxation time of the polymer melt.[41,42] Apparently, in comparison to HDPE, the GF/HDPE melt exhibits "gel" behavior with a significantly increased relaxation time, owing to the good compatibility between the commercial GF and the resin molecular chain through a sizing agent. In the extruding process, the molecular chains in the HDPE melt are disentangled and oriented along the flow field. Subsequently, during the cooling process, this "gel" characteristic places strong restrictions on the relaxation of oriented molecular chains near the interface, and thus, oriented lamellae can be formed. As to the area inside the matrix, random lamellae are generated due to the rapid relaxation of oriented chains.

Based on the discussion of the evolution of GF and matrix morphology above, the schematic diagrams of multiscale microstructures and crack growth in GFPE0 and GFPE20 are illustrated in Figure 12. It is not hard to imagine that the oriented interfacial lamellae endow the composite system with

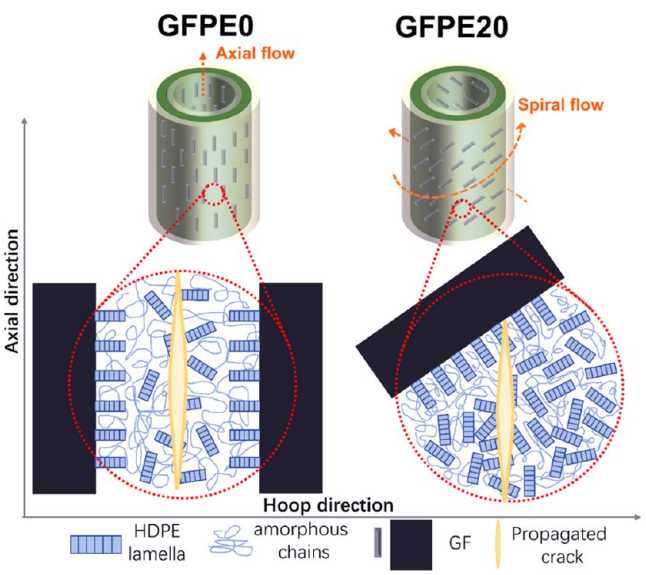


**Figure 12.** Schematic diagram of microstructures and crack growths in GFPE0 and GFPE20.


https://doi.org/10.1021/acs.iecr.1c01455
Ind. Eng. Chem. Res. XXXX, XXX, XXX−XXX

better interfacial properties through mechanical interlocking,[43,44] conducive to the stress transfer between the matrix and fiber;[45] in contrast, it enhances the matrix itself to some extent. The combination of the off-axial fiber and interface lamellae is just like a super-hybrid shish-kebab structure, which overcomes the defect of the fiber length and exerts the orientation reinforcement of fiber as much as possible. In comparison to GFPE0, the super-"hybrid shish-kebab"-like structure, arranged in a bionic spiral formation, improves the hoop bearing capacity for GFPE20 through a remarkable hoop deviation. Also, with the deviated hybrid structure acting as a "roadblock", the axial growth of the crack is blocked and bifurcated to dissipate energy in the bursting test. Despite the axial strength loss by 10.5%, the hoop strength and burst pressure of GFPE20 are enhanced by 25.5 and 24.1%, respectively. These superior performances match the purpose of the study of improving the adaptability of pipe to loading conditions and reducing the long-distance growth risk of the axial crack and also avoid the possible problems in single-layer rotary extruded pipe, such as the conveying resistance caused by the rotating trace and the welding difficulty induced by the floating fiber. Furthermore, it is expected that longer residual fiber may bring greater enhancement anticipate, which will be investigated in our future research.

## 5. CONCLUSIONS

Hoop-reinforced triple-layer HDPE composite pipes with a bionic design strategy of the GF/HDPE middle layer were fabricated through the triple-layer rotating co-extrusion. Inspiringly, the hoop strength and hydraulic damage resistance of GFPE20 are effectively enhanced by 25.5 and 24.1%, respectively, in comparison to those of GFPE0, even with the relatively low aspect ratio of residual fibers. The quantitative relationship between the rotating co-extrusion conditions and multiscale structures including GF and matrix crystals is systematically established via computer simulation. This work sheds light on the formation mechanism of "hybrid shish-kebab" structure and axial crack's "roadblock" for the combination of GF and interfacial lamellae induced by the compound helical shear field, providing effective guidance for the hoop deviation control of multiscale structure in pipe production. Furthermore, it develops a facile hoop-enhancement approach with both academic and industrial value for polyethylene pressure pipes improving the adaptability to production and application requirements.

## ■ ASSOCIATED CONTENT

### Supporting Information

The Supporting Information is available free of charge at https://pubs.acs.org/doi/10.1021/acs.iecr.1c01455.

Flow rate curves along line 1 during the rotating co-extrusion processes (Figure S1); morphologies in the hoop-radial plane and axial-radial plane of the GF/HDPE middle layers (Figure S2); rheological properties of HDPE and GF/HDPE melts at 220 °C (Figure S3); and manufacturers and parameters of extruders (Table S1) (PDF)

## ■ AUTHOR INFORMATION


### Corresponding Author

**Jie Zhang** − *College of Polymer Science and Engineering, State Key Laboratory of Polymer Materials Engineering, Sichuan University, Chengdu 610065, China;* orcid.org/0000-0003-3800-697X; Email: zhangjie@scu.edu.cn; Fax: +86 02885405402

### Authors

**Rui Hong** − *College of Polymer Science and Engineering, State Key Laboratory of Polymer Materials Engineering, Sichuan University, Chengdu 610065, China*

**Menglong Hu** − *College of Polymer Science and Engineering, State Key Laboratory of Polymer Materials Engineering, Sichuan University, Chengdu 610065, China*

**Jin Chen** − *College of Polymer Science and Engineering, State Key Laboratory of Polymer Materials Engineering, Sichuan University, Chengdu 610065, China*

**Qiang Fu** − *College of Polymer Science and Engineering, State Key Laboratory of Polymer Materials Engineering, Sichuan University, Chengdu 610065, China;* orcid.org/0000-0002-5191-3315

Complete contact information is available at: https://pubs.acs.org/10.1021/acs.iecr.1c01455


### Notes

The authors declare no competing financial interest.

## ■ ACKNOWLEDGMENTS

This work was financially supported by the National Natural Science Foundation of China (Grant No. 21627804).

## ■ REFERENCES


(1) Mitroka, S. M.; Smiley, T. D.; Tanko, J. M.; Dietrich, A. M. Reaction mechanism for oxidation and degradation of high density polyethylene in chlorinated water. *Polym. Degrad. Stab.* **2013**, *98*, 1369−1377.

(2) He, X.; Zha, X.; Zhu, X.; Qi, X.; Liu, B. Effect of short chain branches distribution on fracture behavior of polyethylene pipe resins. *Polym. Test.* **2018**, *68*, 219−228.

(3) Kanthabhabha Jeya, R. P.; Bouzid, A.-H. Compression creep and thermal ratcheting behavior of high density polyethylene (HDPE). *Polymers* **2018**, *10*, 156.

(4) Kim, S.; Lee, K. Field performance of recycled plastic foundation for pipeline. *Materials* **2015**, *8*, 2673−2687.

(5) Whelton, A. J.; Dietrich, A. M. Critical considerations for the accelerated ageing of high-density polyethylene potable water materials. *Polym. Degrad. Stab.* **2009**, *94*, 1163−1175.

(6) Sun, N.; Wenzel, M.; Adams, A. Morphology of high-density polyethylene pipes stored under hydrostatic pressure at elevated temperature. *Polymer* **2014**, *55*, 3792−3800.

(7) Maria, R.; Rode, K.; Schuster, T.; Geertz, G.; Malz, F.; Sanoria, A.; Oehler, H.; Brüll, R.; Wenzel, M.; Engelsing, K.; et al. Ageing study of different types of long-term pressure tested PE pipes by IR-microscopy. *Polymer* **2015**, *61*, 131−139.

(8) Kong, C.; Wang, Y.; Ye, L.; Zhao, X. Structure and self-reinforcing mechanism of biaxially oriented polyethylene pipes produced by solid phase die drawing. *Polymer* **2019**, *178*, No. 121556.

(9) Yang, H.; Luo, X.; Shen, K.; Yuan, Y.; Fu, Q.; Gao, X.; Jiang, L. The role of mandrel rotation speed on morphology and mechanical properties of polyethylene pipes produced by rotational shear. *Polymer* **2019**, *184*, No. 121915.

(10) DiBenedetto, A. T. Tailoring of interfaces in glass fiber reinforced polymer composites: a review. *Mater. Sci. Eng., A* **2001**, *302*, 74−82.

(11) Abrão, A. M.; Faria, P. E.; Rubio, J. C. C.; Reis, P.; Davim, J. P. Drilling of fiber reinforced plastics: A review. *J. Mater. Process. Technol.* **2007**, *186*, 1−7.

(12) Martin, J. J.; Fiore, B. E.; Erb, R. M. Designing bioinspired composite reinforcement architectures via 3D magnetic printing. *Nat. Commun.* **2015**, *6*, No. 8641.
(13) Zhang, X.; Xie, J.; Chen, J.; Okabe, Y.; Pan, L.; Xu, M. The beetle elytron plate: a lightweight, high-strength and buffering functional-structural bionic material. *Sci. Rep.* **2017**, *7*, No. 4440.
(14) Grunenfelder, L.; Suksangpanya, N.; Salinas, C.; Milliron, G.; Yaraghi, N.; Herrera, S.; Evans-Lutterodt, K.; Nutt, S.; Zavattieri, P.; Kisailus, D. Bio-inspired impact-resistant composites. *Acta Biomater.* **2014**, *10*, 3997−4008.
(15) Weaver, J. C.; Milliron, G. W.; Miserez, A.; Evans-Lutterodt, K.; Herrera, S.; Gallana, I.; Mershon, W. J.; Swanson, B.; Zavattieri, P.; DiMasi, E.; et al. The stomatopod dactyl club: a formidable damage-tolerant biological hammer. *Science* **2012**, *336*, 1275−1280.
(16) Zhang, K.; Li, X.; Nie, M.; Wang, Q. Helical flow-driven alignment of off-axial silver-functionalized titanium dioxide fibers in polypropylene tube suitable for medical applications. *Compos. Sci. Technol.* **2018**, *158*, 121−127.
(17) Yilmaz, O.; Kısasöz, E.; Seniha Guner, F.; Nart, C.; Kirkkopru, K. A comprehensive 3D analysis of polymer flow through a conical spiral extrusion die. *Fibers Polym.* **2014**, *15*, 84−90.
(18) Nie, Y.; Hao, J.; Lin, Y.-J.; Sun, W. 3D simulation and parametric analysis of polymer melt flowing through spiral mandrel die for pipe extrusion. *Adv. Polym. Technol.* **2018**, *37*, 3882−3895.
(19) Li, Y.; Nie, M.; Wang, Q. Facile Fabrication of Electrically Conductive Low-Density Polyethylene/ Carbon Fiber Tubes for Novel Smart Materials via Multiaxial Orientation. *ACS Appl. Mater. Interfaces* **2018**, *10*, 1005−1016.
(20) Li, Y.; Zhang, K.; Nie, M.; Wang, Q. Tubular Sensor with Multi-Axial Strain Sensibility and Heating Capability Based on Bio-Mimic Helical Networks. *Ind. Eng. Chem. Res.* **2019**, *58*, 22273−22282.
(21) Zhang, K.; Li, Y.; Zhou, H.; Nie, M.; Wang, Q.; Hua, Z. Polyurethane/carbon fiber composite tubular electrode featuring three-dimensional interpenetrating conductive network. *Carbon* **2018**, *139*, 999−1009.
(22) Nie, M.; Wang, Q.; Bai, S. Morphology and property of polyethylene pipe extruded at the low mandrel rotation. *Polym. Eng. Sci.* **2010**, *50*, 1743−1750.
(23) Han, R.; Nie, M.; Bai, S.; Wang, Q. Control over crystalline form in polypropylene pipe via mandrel rotation extrusion. *Polym. Bull.* **2013**, *70*, 2083−2096.
(24) Nie, M.; Han, R.; Wang, Q. Formation and alignment of hybrid shish-kebab morphology with rich beta crystals in an isotactic polypropylene pipe. *Ind. Eng. Chem. Res.* **2014**, *53*, 4142−4146.
(25) Liu, W.; Nie, M.; Wang, Q. Biaxial reinforcements for polybutene-1 medical-tubes achieved via flow-design controlled morphological development of incorporated polystyrene: In-situ microfibrillation, alignment manipulation and performance optimization. *Compos. Sci. Technol.* **2015**, *119*, 124−130.
(26) Deng, C.; Jin, B.; Zhao, Z.; Shen, K.; Zhang, J. The influence of hoop shear field on the structure and performances of glass fiber reinforced three-layer polypropylene random copolymer pipe. *J. Appl. Polym. Sci.* **2019**, *136*, No. 46985.
(27) Sockalingam, S.; Dey, M.; Gillespie, J. W.; Keefe, M. Finite element analysis of the microdroplet test method using cohesive zone model of the fiber/matrix interface. *Composites, Part A* **2014**, *56*, 239−247.
(28) Ren, D.; Li, K.; Chen, L.; Chen, S.; Han, M.; Xu, M.; Liu, X. Modification on glass fiber surface and their improved properties of fiber-reinforced composites via enhanced interfacial properties. *Composites, Part B* **2019**, *177*, No. 107419.
(29) Chin, W.-K.; Liu, H.-T.; Lee, Y.-D. Effects of fiber length and orientation distribution on the elastic modulus of short fiber reinforced thermoplastics. *Polym. Compos.* **1988**, *9*, 27−35.
(30) Bajracharya, R. M.; Manalo, A. C.; Karunasena, W.; Lau, K.-t. Experimental and theoretical studies on the properties of injection moulded glass fibre reinforced mixed plastics composites. *Composites, Part A* **2016**, *84*, 393−405.
(31) Vaxman, A.; Narkis, M.; Siegmann, A.; Kenig, S. Short-Fiber Thermoplastics Composites: Fiber Fracture During Melt Processing. In *Wiley Encyclopedia of Composites*; John Wiley & Sons, 2011; pp 1−19.
(32) Shah, D. U. Developing plant fibre composites for structural applications by optimising composite parameters: a critical review. *J. Mater. Sci.* **2013**, *48*, 6083−6107.
(33) Kelly, A.; Tyson, W. R. Tensile properties of fibre-reinforced metals: Copper/tungsten and copper/molybdenum. *J. Mech. Phys. Solids* **1965**, *13*, 329−350.
(34) Facca, A. G.; Kortschot, M. T.; Yan, N. Predicting the tensile strength of natural fibre reinforced thermoplastics. *Compos. Sci. Technol.* **2007**, *67*, 2454−2466.
(35) Wang, T.; Li, N.; Link, G.; Jelonnek, J.; Fleischer, J.; Dittus, J.; Kupzik, D. Load-dependent path planning method for 3D printing of continuous fiber reinforced plastics. *Composites, Part A* **2021**, *140*, No. 106181.
(36) Mi, D.; Xia, C.; Jin, M.; Wang, F.; Shen, K.; Zhang, J. Quantification of the effect of shish-kebab structure on the mechanical properties of polypropylene samples by controlling shear layer thickness. *Macromolecules* **2016**, *49*, 4571−4578.
(37) Hou, F.; Mi, D.; Zhou, M.; Zhang, J. The influences of a novel shear layer-spherulites layer alternated structure on the mechanical properties of injection-molded isotactic polypropylene. *Polymer* **2017**, *122*, 12−21.
(38) Chen, Y.; Bo, X.; Yang, S.; Yang, H.; Lawson, T.; Wu, Z.; Zhang, Q.; Li, Z. Unexpected Strength and Toughness Reinforcement of the Injection-Molded Isotactic Polypropylene Parts with Oriented *β*-Crystals. *Ind. Eng. Chem. Res.* **2017**, *56*, 14252−14262.
(39) Gu, X.; Wang, Y.; Jiang, Y.; Liu, M.; Fu, Q.; Zhang, J. High impact performance induced by a synergistic effect of heteroepitaxy and oriented layer-unoriented layer alternated structure in iPP/HDPE injection molded part. *Polymer* **2019**, *175*, 206−214.
(40) Wang, H.; An, C.; Duan, M.; Su, J. Transient thermal analysis of multilayer pipeline with phase change material. *Appl. Therm. Eng.* **2020**, *165*, No. 114512.
(41) Wang, J.; Benyahia, L.; Chassenieux, C.; Tassin, J.-F.; Nicolai, T. Shear-induced gelation of associative polyelectrolytes. *Polymer* **2010**, *51*, 1964−1971.
(42) Vega, J. F.; Rastogi, S.; Peters, G. W. M.; Meijer, H. E. H. Rheology and reptation of linear polymers. Ultrahigh molecular weight chain dynamics in the melt. *J. Rheol.* **2004**, *48*, 663−678.
(43) Zhang, K.; Li, Y.; He, X.; Nie, M.; Wang, Q. Mechanical interlock effect between polypropylene/ carbon fiber composite generated by interfacial branched fibers. *Compos. Sci. Technol.* **2018**, *167*, 1−6.
(44) Ning, N.; Fu, S.; Zhang, W.; Chen, F.; Wang, K.; Deng, H.; Zhang, Q.; Fu, Q. Realizing the enhancement of interfacial interaction in semicrystalline polymer/filler composites via interfacial crystallization. *Prog. Polym. Sci.* **2012**, *37*, 1425−1455.
(45) Shi, S.; Wang, L.; Pan, Y.; Liu, C.; Liu, X.; Li, Y.; Zhang, J.; Zheng, G.; Guo, Z. Remarkably Strengthened microinjection molded linear low-density polyethylene (LLDPE) via multi-walled carbon nanotubes derived nanohybrid shish-kebab structure. *Composites, Part B* **2019**, *167*, 362−369.


https://doi.org/10.1021/acs.iecr.1c01455
*Ind. Eng. Chem. Res.* XXXX, XXX, XXX−XXX